JOURNAL OF MATERIALS SCIENCE 30 (1995) 3222–3230

Microstructure development of Si_3N_4–TiN composite prepared by *in situ* compositing

C. M. WANG*
School of Materials, University of Leeds, Leeds, LS2 9JT, UK

Si_3N_4–TiN nano-composite has been prepared by an *in situ* compositing method with silicon nitride powder, aluminium iso-propoxide and titanium butoxide as the raw materials. The densification mechanism during hot-pressing and the microstructure of the densified materials were characterized from the point of view of phase composition, TiN inclusion distribution and the interface properties. The dense materials were mainly composed of β′-sialons, residual α-Si_3N_4, silicon oxynitride, and TiN. The materials were featured by the very fine size of the precursor-derived particulate TiN which was homogeneously distributed in the matrix.

1. Introduction

The incorporation of titanium nitride and titanium carbide as particulate second phases into a silicon nitride matrix has received attention with a view to improving the fracture toughness and strength [1–3]. The degree of toughening obtained and the reliability of the composite, are strongly controlled by microstructure, defined in terms of matrix grain size, morphology and distribution, and inclusion size and distribution, together with possible interactions between the inclusion phase and the matrix [4, 5]. The preparation of a particulate composite by conventional powder processing always generates relatively large agglomerates and/or inclusions of one phase and, hence limits the degree of microstructural homogeneity. A development in the processing of this kind of material, has been terminated "*in situ* compositing". This comprises using a precursor phase which can be homogeneously incorporated in the green body and then transformed to inclusion particles by a reaction or precipitation process during the sintering stage. A well-established example is provided by the Si_3N_4–SiC composite system [6], in which SiC particles are formed *in situ* from a polysilane. The advantage of *in situ* compositing can be seen in the fine inclusion particle size and in the homogeneous distribution of the inclusions in the matrix. Ovreboe *et al.* [7] have systematically studied the effectiveness of the mixed oxide system Al_2O_3–SiO_2–TiO_2 on the densification of Si_3N_4 by hot-pressing. At a constant 10% by weight total addition, the proportions of Al_2O_3 and TiO_2 added to the Si_3N_4 powder were varied within the ratio range 0:1 to 1:0, as shown on the Al_2O_3–SiO_2–TiO_2 ternary diagram in Fig. 1. The overall best compositional range giving both high densification rate and final density appeared to be Al_2O_3/TiO_2 = 3:2 to 10:0, and it appeared that the highest densification rates corresponded to the composition with a ratio of $Al_2O_3/TiO_2 = \sim 7:3$ by weight, although this particular composition was not actually used in the previous study. On this basis, the composition of 7 wt% Al_2O_3 and 3 wt% TiO_2 was chosen for the present study. Here we report the *in situ* preparation and microstructural characterization of a silicon nitride material dispersed with nano-size TiN particulate inclusions, using titanium butoxide as precursor.

2. Experimental procedure

Silicon nitride powder (Starck, LC12-N, Berlin), with a sedimentation mean particle size of 500 nm, nitrogen adsorption specific surface area of 17.4 m^2g^{-1}, initial α-silicon nitride content of 96%, and an oxygen content of 1.58 wt% (manufacturer's data), was hot pressed with 3 wt% TiO_2 and 7 wt% Al_2O_3 sintering additive system, introduced by a particle coating process, as reported elsewhere [8]. The overall starting composition is shown in Table I, which is also shown in both the Al_2O_3–TiO_2–SiO_2 phase diagram (point c in Fig. 1), and the Si_3N_4–Al_2O_3–SiO_2 –AlN phase diagram (point s in Fig. 2). The blended powder was hot-pressed at 1700 °C, and 20 MPa for periods of 0.46, 1.6 and 5.4 ks. The shrinkage of the samples was continuously monitored by a transducer and the data were collected by computer.

The products phase composition was analysed by X-ray diffraction (XRD) using powders prepared by crushing hot-pressed discs in a tungsten carbide-lined mill. 10 wt% ~200 μm silicon powder was used as internal standard, with CuK_α radiation on a Philips APD1750 automatic powder diffraction system. The

*Present address: Max Planck-Institute für Metallforschung, See Strasse 92, D-70174, Stuttgart, Germany.

0022–2461

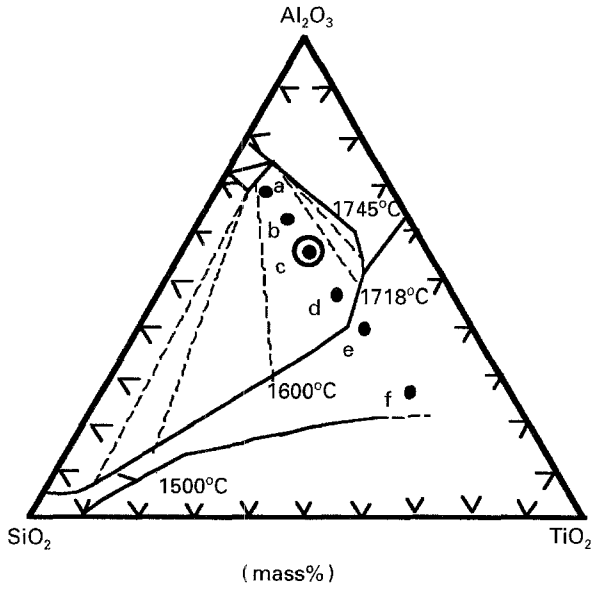

Figure 1 The Al_2O_3–SiO_2–TiO_2 ternary diagram. The compositions shown are weight percentage of (Al_2O_3, TiO_2) (a) (9, 1), (b) (8, 2), (c) (7, 3), (d) (6, 4), (e) (5, 5), (f) (3, 7), assuming 3 wt% SiO_2 is present on the Si_3N_4 particle surfaces [7].

TABLE I The starting composition of the powder for hot-pressing

	(wt %)	(mol %)
Si_3N_4	87	80
Al_2O_3	7	9
TiO_2	3	5
SiO_2[a]	3	6

[a] Assuming silica is present on the Si_3N_4 particle surfaces.

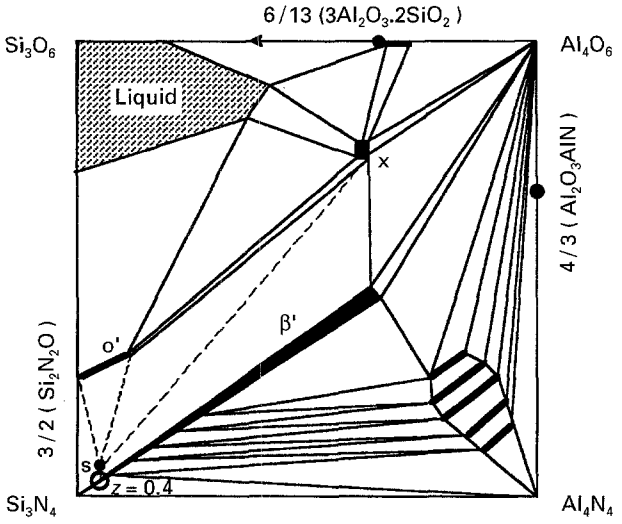

Figure 2 The system Si_3N_4–SiO_2–Al_2O_3–AlN [38].

sample was scanned for a 2θ of ~10°–80° with a scanning speed of 2θ 0.01° s^{-1}. The relative contents of the α- and β-phases were determined by the method proposed by Gazzara and Messier [9, 10]

$$\alpha = (-0.443R_\alpha^2 + 1.443R_\alpha) \quad (1)$$

$$R_\alpha = \frac{I_{\alpha(2\,1\,0)}}{I_{\alpha(2\,1\,0)} + I_{\beta(2\,1\,0)}} \quad (2)$$

where $I_{\alpha(2\,1\,0)}$ and $I_{\beta(2\,1\,0)}$ are the integrated α- and β-phase (2 1 0) peak intensities.

The relative contents of TiN and Si_2N_2O were also estimated by the integrated peak intensity method [11]

$$w_i = \frac{I_i}{\sum I_i} \quad (3)$$

where w_i is the fraction weight of phase i, I_i is the integrated intensity of phase i; α-Si_3N_4(2 1 0), β-Si_3N_4(2 1 0), Si(1 1 1), TiN(2 0 0) and Si_2N_2O(2 0 0) peaks were used.

The lattice parameters of β′-sialon were calculated from the equation for a hexagonal cell

$$\frac{1}{d^2} = \frac{4}{3}\left(\frac{h^2 + hk + k^2}{a^2}\right) + \frac{l^2}{c^2} \quad (4)$$

where ($h\,k\,l$) are the Miller indices, d is the lattice planar distance and a and c are the hexagonal lattice parameters. The (2 1 0) and (1 0 1) peaks were used to calculate a and c; d was calculated using the Bragg equation with 2θ calibrated by the silicon (1 1 1) peak with a lattice parameter of 543.01 pm (JCPDS card 5-655). The sialon z-value used is the average of two values obtained from the a and c cell dimensions using the following equation [12]

$$a = 760.3 + 2.96z \text{ pm} \quad (5)$$

$$c = 290.7 + 2.55z \text{ pm} \quad (6)$$

Thin foils for transmission electron microscopy (TEM) were prepared by diamond slitting and hand thinning of the hot-pressed sample to a thickness of 30 μm, followed by ion-beam milling using 4 kV argon ions incident on both surfaces of the foil at an angle of 20°, until perforation. 10° milling was continued for 2 h to increase the area of electron transparency. The thin foils were examined in a Jeol 200 CX TEM/STEM instrument, operating at 200 kV, with an attached Link EDS system for elemental analysis. High-resolution TEM was carried out on a Philips EM430 with an accelerating voltage of 300 kV.

3. Results

3.1. Phase composition

Continuous monitoring of powder shrinkage established that full density was reached in 240 s (Fig. 3). The resulting material was composed mainly of α-Si_3N_4 and β′-Si_3N_4, also lesser amounts of Si_2N_2O and TiN as determined by XRD. There was an extremely small amount of glass segregated in the grain junction which could be identified by centralized dark-field imaging (CDF) under TEM. Fig. 4 shows the proportions of crystalline phases as a function of hot-pressing time. The amount of α-Si_3N_4 decreased with time, while β′-Si_3N_4 increased. The amount of Si_2N_2O and TiN initially increased rapidly and reached a plateau after about 1600 s.

The z value of the β′-Si_3N_4 phase as a function of hot-pressing time is shown in Fig. 5. The z value

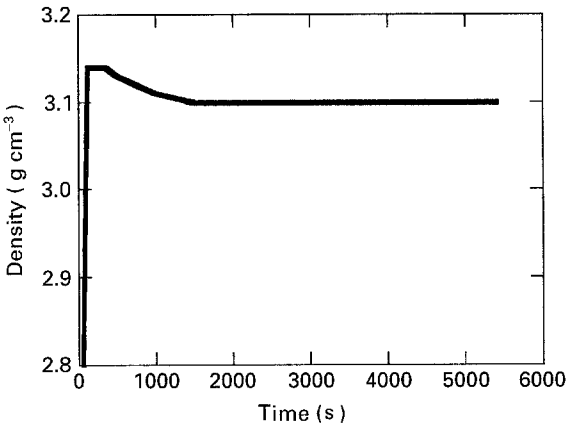

Figure 3 Density as a function of time at 1700 °C and 20 MPa.

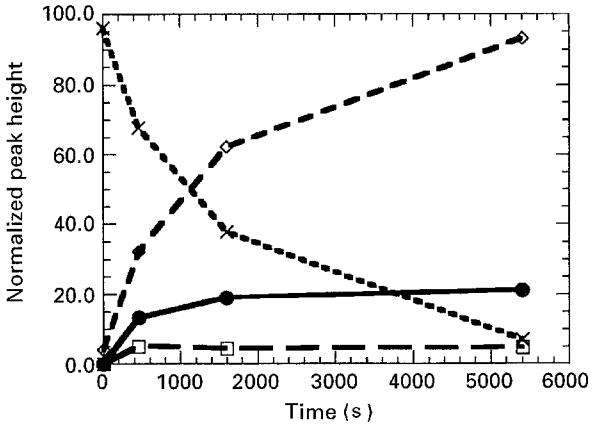

Figure 4 Normalized X-ray peak heights as a function of time after hot-pressing at 1700 °C and 20 MPa. (-●-) Si_2N_2O, (-□-) TiN, (--◇--) α-Si_3N_4, (-- × --) β-Si_3N_4.

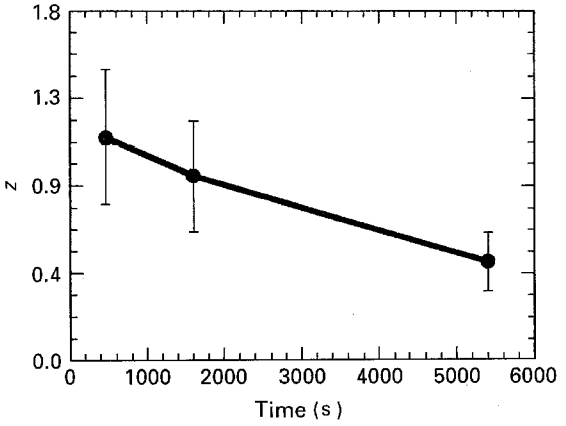

Figure 5 z-value as a function of time after hot-pressing at 1700 °C and 20 MPa.

decreased markedly with time, indicating the rapid redistribution of aluminium between the intergranular and primary phases as previously observed in the sintering of β′-sialon [13]. After 5.4 ks the z value reached 0.5, and appeared to be still slowly decreasing, as the theoretical value should be 0.38 with all of the aluminium in the silicon nitride lattice.

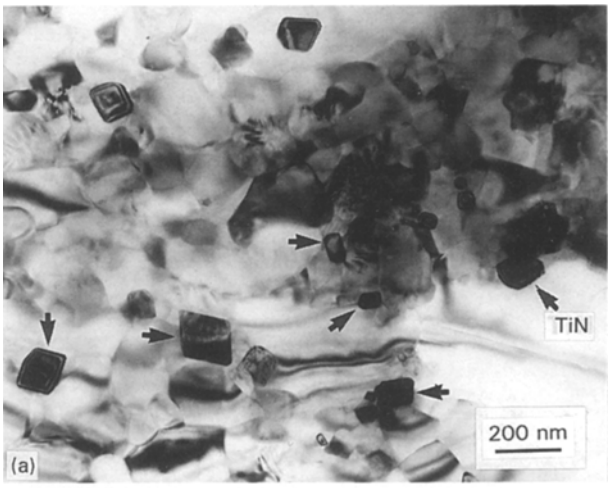

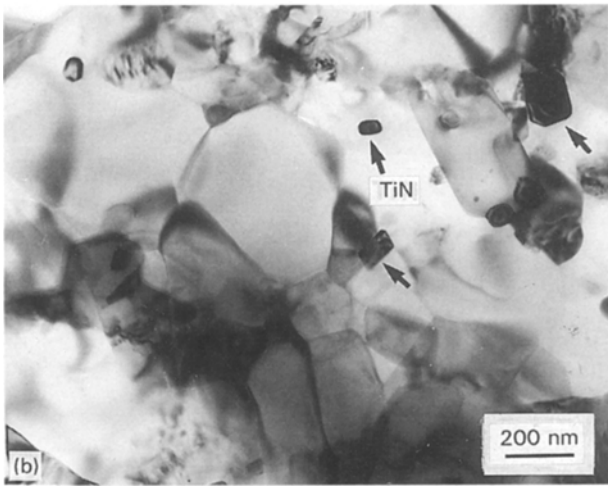

Figure 6 Transmission electron micrographs of general views of the microstructure of 1700 °C and 20 MPa hot-pressed materials: (a) 460 s, (b) 5.4 ks.

3.2. Microstructure characterization

3.2.1. General morphology

The microstructure of the hot-pressed silicon nitride generally consisted of equiaxed β′-Si_3N_4 grains, coordinated either by β′-Si_3N_4 grains or by other crystalline phases such as TiN, Si_2N_2O, and α-Si_3N_4 or by an amorphous phase as shown in Fig. 6. The β′-Si_3N_4 had a grain size of 100–1000 nm after 460 s and 200–1500 nm after 5.4 ks.

3.2.2. Silicon oxynitride (Si_2N_2O)

The Si_2N_2O was present as relatively large, elongated grains as shown typically in Fig. 7. These grains were identified by selected-area electron diffraction in the TEM and generally had a faulted structure, as shown by the streaking of diffraction spots. This represents a relaxation of the Laue diffraction condition for the faulted planes in certain orientations, and can also be used to distinguish Si_2N_2O from Si_3N_4 in TEM images [14]. Stacking faults are parallel to the (1 0 0) planes, which are linked by the relatively weak Si–O–Si bonds in the orthorhombic crystal. This plane has the lowest stacking fault energy and the faults are introduced randomly during the addition of

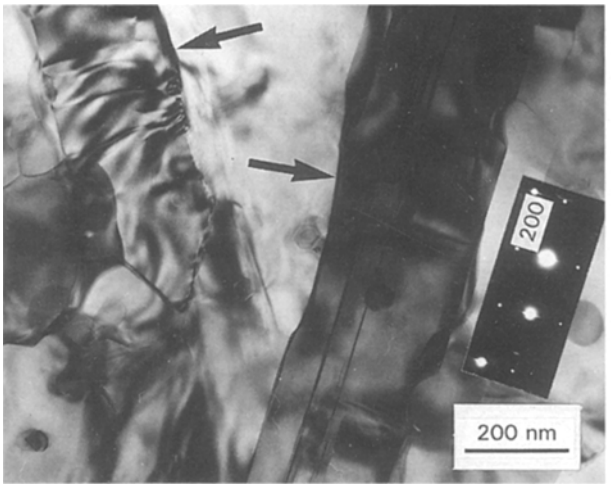

Figure 7 Transmission electron micrograph showing typical Si_2N_2O grains (arrowed) after 5.4 ks.

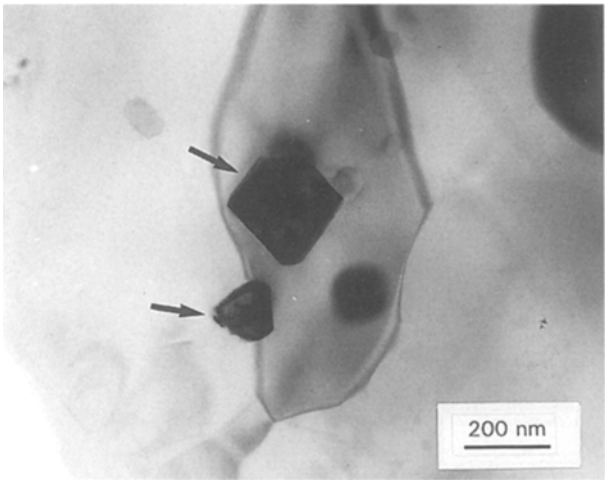

Figure 8 Transmission electron micrograph showing the intragranular distribution of TiN (arrowed), after 5.4 ks.

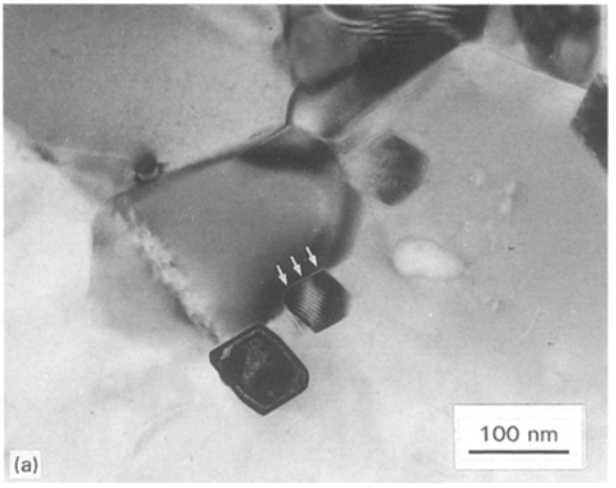

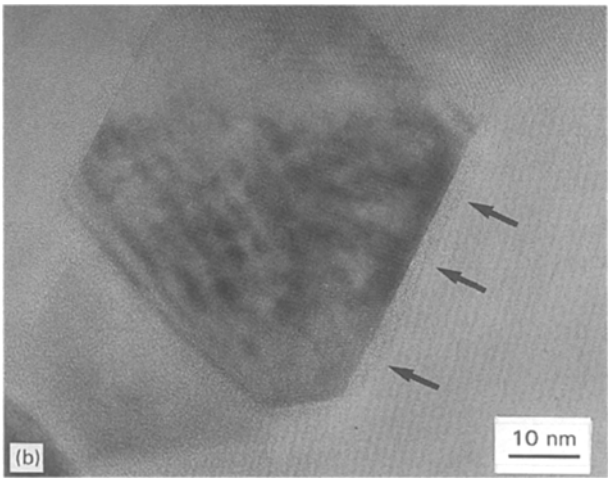

Figure 9 Transmission electron micrographs showing the growth of β-Si_3N_4 grains at the expense of α-Si_3N_4 after 460 s: (a) general view, (b) high-resolution image with a glass film of 3 nm resolved (arrowed).

successive atomic planes during crystal growth from the sintering liquid. The (1 0 0) fault planes are also those with the lowest solid–liquid surface energy and hence are amplified during grain growth. Some Si_2N_2O grains contained particles of other crystalline phases, such as Si_3N_4 and TiN. Some Si_2N_2O pockets with an irregular grain shape were also seen.

3.2.3. TiN

The TiN particles could be identified in the material either by electron diffraction, or more readily by the darker contrast of TiN as a result of the stronger electron absorption of the heavier titanium. TiN particles with sizes ranging from 20–200 nm were distributed both intergranularly, and intragranularly within Si_3N_4 or Si_2N_2O grains, as shown in Fig. 8. The small size of the TiN particle is a direct consequence of the fine scale of the TiO_2 starting particles derived from the hydrolysis of alkoxide of $\sim$10–50 nm, and also slight grain coarsening occurs during heating to the sintering temperature. A careful check of the interface between Si_3N_4 grains and different sizes of TiN inclusion up to 200 nm showed no evidence of microcracking, either within the Si_3N_4 and TiN grains or at the boundary, although this might have been expected as a result of thermal mismatch between Si_3N_4 and TiN. However, a typical feature is the imperfection of the TiN grains under TEM, a very high density of dislocation damage, where the dislocations were introduced as a result of electron radiation, by ion-beam thinning, or the thermal mismatch stress; this is still unclear.

3.2.4. Amorphous phase

TEM and HRTEM observation of the 460 and 5.4 ks hot-pressed materials showed that the volume fraction of residual glass was extremely low. The distribution of this phase could be described in terms of two features: firstly, irrespective of hot-pressing time, all crystalline phases were separated by a 2–3 nm thickness of glass film (Fig. 9); secondly, in the 460 s hot-pressed materials, there was an occasional large glass pocket of around 100 nm (Fig. 10). After 5.4 ks, the relatively large glass pockets could not be detected and instead a crystalline phase developed with a conical shape morphology wedged between three and

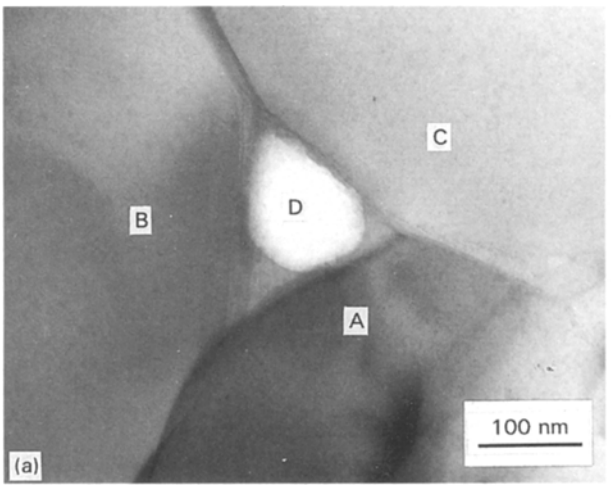

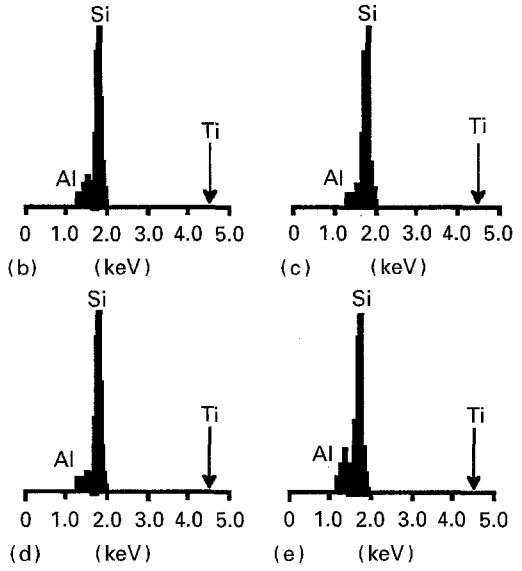

Figure 10 Transmission electron micrographs showing the presence of glass pockets (D) at grain junctions with a size of 100 nm after 460 s: (a) bright field, (b–d) EDS corresponding to different grains in (a).

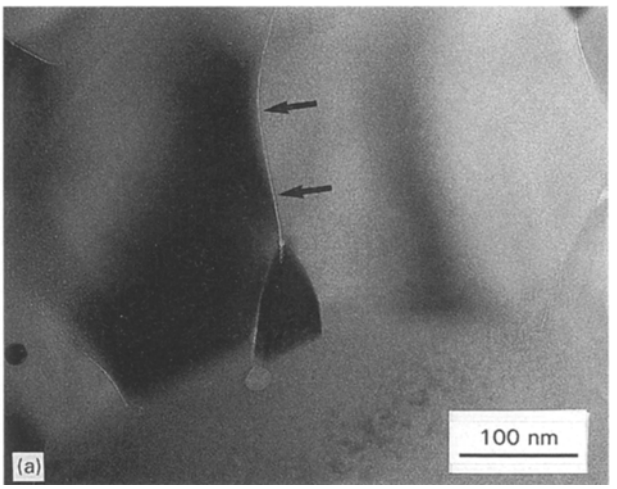

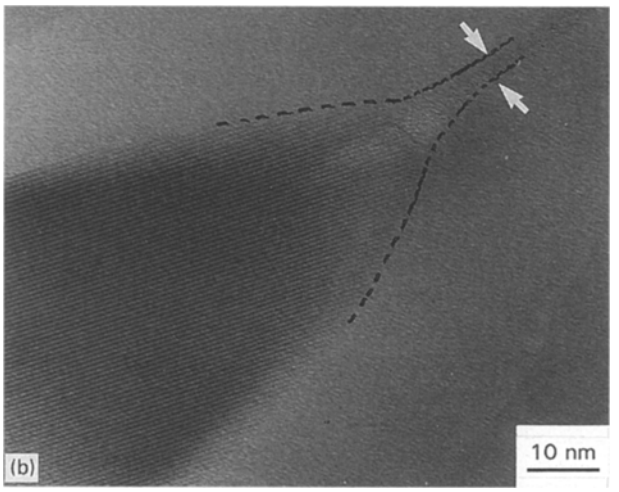

Figure 11 Transmission electron micrographs showing a crystallized glass pocket with the tail remaining as a glass film (arrowed) between two grains: (a) bright field, (b) high-resolution image.

multi-grain junctions, as shown in Fig. 11. Under the special imaging conditions (diffraction spot and the glass diffuse ring overlap), crystalline phase could be seen to be still connected to the remaining intergranular glass.

4. Discussion

4.1. Densification mechanism

In practice, the Al_2O_3–SiO_2–TiO_2 system added at the level of $\sim 13\%$ (assuming $\sim 3.0\%$ SiO_2 to be present on the Si_3N_4 particle surface) allows for satisfactory hot-pressing densification of sub-micrometer Si_3N_4 powders. The Si_3N_4 densification process using a liquid based on the Al_2O_3–SiO_2–TiO_2 system can be broadly described by the three successive steps of Kingery's model for liquid-phase sintering [15], namely particle rearrangement, solution of α-Si_3N_4 in the liquid, and the crystallization of β'-Si_3N_4 through adsorption of Al_2O_3 from the liquid phase. The general requirement for a liquid-phase sintering medium is that there is a sufficient volume fraction of liquid phase which completely wets the solid phase, and that the solid phase has an appreciable solubility in the liquid. The nature of the metal oxide sintering additive system determines the eutectic temperature and also the volume fraction and viscosity of liquid phase formed at the densification temperature [16, 17]. During consolidation of Si_3N_4 by hot-pressing, the applied pressure accelerates densification significantly, and because of the short time required to attain full density, phase equilibrium may not be attained by the solution and recrystallization. This results in a certain amount of retained, lower stability, α-Si_3N_4 in the fully dense material, as seen in dense material formed with only 460 s hot-pressing. With further heating, the solution–recrystallization process continues, and the degree of α-Si_3N_4 to β'-Si_3N_4 conversion depends on the properties of the liquid, and the time available.

The Al_2O_3–SiO_2–TiO_2 phase diagram may provide an approximate guide to the initial liquid-forming behaviour of this system (Fig. 1), but it cannot be applied too rigorously because of the progressive reduction of TiO_2 to Ti_5O_9, Ti_4O_7, Ti_3O_5 and finally TiO (this can be generally expressed as $TiO_{(2-x)}$) under the low oxygen potential conditions of the sintering environment of Si_3N_4 and a graphite die,

completed by reactions of the titanium oxides with Si_3N_4 or nitrogen to form TiN [18, 19]. Because no compounds form in the TiO_2–SiO_2 system, and the continuous reduction of the TiO_2, the function of the TiO_2 will be complex during the densification process. A parallel can be seen in the Si_3N_4 densification system Fe_2O_3–SiO_2. Although there are no compounds to form in the Fe_2O_3–SiO_2 system, the continuing reduction of Fe_2O_3 to FeO leads to the binary eutectics in the FeO–SiO_2 system at 1178 °C [20].

In the Al_2O_3–SiO_2–Si_3N_4 system, the eutectic temperature is 1470 °C [21]. The Al_2O_3–SiO_2–TiO_2 system has a eutectic temperature of 1480 °C. The reduction of TiO_2 to $TiO_{(2-x)}$ is likely to reduce the liquid-formation temperature. A eutectic temperature of $\ll$ 1480 °C may be expected in the case of the quaternary system also involving Si_3N_4. The overall densification process thus can be described as follows.

(i) During heating, in the temperature range 1100–1480 °C, TiO_2 will be progressively reduced to $TiO_{(2-x)}$, and subsequently reacts with Si_3N_4 to form TiN [18], likely reactions are

$$2TiO_2(s) \rightarrow 2TiO_{(2-x)} + xO_2(g) \quad (7)$$

$$6Ti_3O_5(s) + 5Si_3N_4(s) \rightarrow 18TiN(s) + 15SiO_2 + N_2 \quad (8)$$

The extent of reduction of the TiO_2 to $TiO_{(2-x)}$ and finally to TiN depends on the reaction temperature and time available [7, 18, 22–25]. On the basis of the rate of the carbothermal reduction of TiO_2 (particle size ~10 nm) to TiN at 1400 °C, and the results of Trigg and McCartney [22] concerning the reaction of Si_3N_4 with TiO_2 at temperatures from 1100–1500 °C, the time for complete reduction of TiO_2 to TiN at 1400 °C is estimated to be ~5 ks. The time required during heating from 1100–1480 °C is ~500 s. Although the exact amount of TiN formed during this heating period was not determined, a possible estimate can be made following the linear relationship between the extent of conversion and time in the carbothermal nitridation of TiO_2 [19]. Thus, it is estimated that 10% of the TiO_2 could be reduced to TiN during this heating period. The reduction of TiO_2 to TiN and the SiO_2 produced (Reactions 7 and 8) during this period will be expected to shift the liquid composition towards the side richer in SiO_2 (Fig. 12 is a schematic drawing of the densification process).

(ii) At the liquid temperature, the SiO_2 on the Si_3N_4 particle surfaces will react with the Al_2O_3 and titanium oxide to form a liquid. Simultaneously, the dissolved TiO_2 in the liquid will be expected to both react with Si_3N_4 at the Si_3N_4–liquid interface to form TiN and SiO_2, and to precipitate on the TiN nuclei produced during the heating process. The overall lifetime of TiO_2 is estimated to be shorter than 1.3 ks during the hot-pressing process (the heating period from 1100–1700 °C is ~800 s, and after 460 s at 1700 °C, the TiO_2 to TiN conversion is completed, based on XRD analysis, Fig. 4) [19]. The rapid conversion of TiO_2 to TiN in the present hot-pressing system is supported by the fact that the residual glass

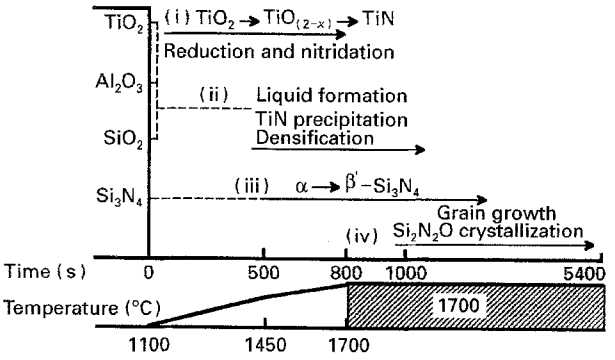

Figure 12 A schematic drawing of the densification process corresponding to (i)–(iv) in the text.

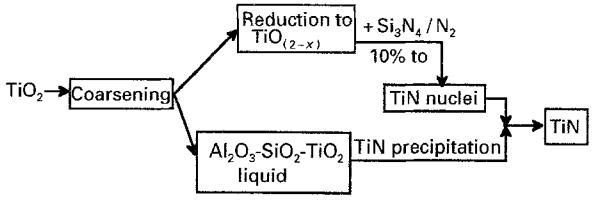

Figure 13 A schematic drawing showing the conversion of TiO_2 to TiN through two routes.

pockets in material hot-pressed only for 460 s show no detectable titanium content by EDS in TEM (Fig. 10). With progression of Reaction 8, the liquid composition is therefore assumed to be continuously being depleted in titanium and enriched in SiO_2. From this liquid, $3Al_2O_3 \cdot 2SiO_2$ (mullite) may, in theory, be expected to nucleate. However, it has been found in practice that this nucleation is very difficult [26, 27]. In the present hot-pressed materials, mullite was not detected by XRD. The two conversion routes of TiO_2 to TiN are schematically shown in Fig. 13.

(iii) At the same time, the reconstructive α-Si_3N_4 to β′-Si_3N_4 phase transformation occurs through solution of the α-phase, and reprecipitation as a β-phase, and is accompanied by the incorporation of aluminium and oxygen atoms into the lattice by Reaction 9, then forming a β′-sialon

$$(8 - z)Si_3N_4 + 2zAl_2O_3 \rightarrow 4Si_{6-z}Al_zO_zN_{8-z} + zSiO_2 \quad (9)$$

(iv) With progression of Reactions 8 and 9, the liquid volume would be expected to decrease, and the remainder of the liquid shifts towards a SiO_2-rich composition approaching the Si_3N_4–SiO_2 boundary of the Si_3N_4–SiO_2–Al_2O_3–AlN behaviour diagram (Fig. 2). There are two immediate consequences of this shift: firstly, there would be an increase in the viscosity of the liquid, and secondly, Si_2N_2O is expected to be formed by the reaction

$$Si_3N_4 + SiO_2 \rightarrow 2Si_2N_2O \quad (10)$$

Reaction 10 will cause a further decrease in the liquid volume. The crystallization of Si_2N_2O from the liquid phase is indicated by the characteristically faulted (1 0 0) planes, and by the fact that the Si_2N_2O grains envelop other crystalline phases (Fig. 7). The

(1 0 0) plane corresponds to the lowest solid–liquid surface energy [14]. The growth of the Si_2N_2O preferentially in the [0 0 1] direction causes the development of a high aspect ratio grain.

Assuming that Reactions 8–10 occur, the final proportions of TiN and Si_2N_2O, and the β′-sialon z-value can be calculated. The maximum content of TiN should be ~2.4 wt%, that of Si_2N_2O ~9.1 wt%, with the β′-sialon having a z-value ~0.4. The calculated z-value is consistent with the experimentally measured value of ~0.5 after 5.4 ks. A quantitative phase content composition analysis was not possible because of the lack of standard samples.

The observed slight decrease of bulk density following the initial hot-pressing density maximum can be ascribed to two factors: the solid solution of aluminium and oxygen into the Si_3N_4 lattice inducing lattice expansion, and the formation of Si_2N_2O of density 2.82 g cm^{-3}. The volume expansion from Reaction 7 is 2.5% (density values of Si_3N_4, 3.20 g cm^{-3}, TiO_2, 4.24 g cm^{-3}, TiN, 5.4 g cm^{-3}, and SiO_2, 2.20 g cm^{-3}), that from Reaction 8 is 2.6% (Al_2O_3, 3.98 g cm^{-3}) for a z-value of 0.4, and that from Reaction 9 is 6.9% (Si_2N_2O, 2.82 g cm^{-3}). With the phase contents of TiN 2.4%, Si_2N_2O 9.1% and β′-sialon (of z-value 0.4) 89.5%, the estimated total volume expansion is thus ~3.0%. This value is close to the experimentally observed volume expansion of ~1.3% (in Fig. 3 a maximum density of 3.14 g cm^{-3}, and final density of 3.10 g cm^{-3} are obtained). The solid solution of aluminium and oxygen into the Si_3N_4 (Reaction 9) contributes most to the volume expansion (as the β′-sialon is the major phase). The difference in the volume expansion between the calculated and observed values may result from the approximation made in calculating the β′-sialon z-value, that all the added aluminium enters the Si_3N_4 lattice; however, the residual glass phase segregated in the grain boundary is still aluminium-containing, as shown by EDS in STEM (Fig. 10).

4.2. The role of TiN

On the basis of the carbothermal nitridation of TiO_2 to TiN, the size and morphology of TiN was closely related to that of the TiO_2 particles [19]. In the present case, the TiN particle size is much larger than the initial coating TiO_2 particle size (~10 nm). This is possibly a result of partially coarsening of the TiO_2 during heating to the hot-pressing temperature, and partially to precipitation of TiN from the liquid. The size distribution of the TiN particles shows no apparent change with hot-pressing time between 460 s and 5.4 ks. The absence of any visible coarsening of the TiN particles at longer hot-pressing times is likely to be a consequence of the homogeneous distribution of a small volume of TiN particles which are completely isolated by Si_3N_4 grains, and of an apparently low solubility of TiN in the liquid.

During densification, the particulate TiN formed by nitridation of TiO_2 during heating and precipitation from the liquid, is likely to affect the subsequent densification and grain-growth processes of the Si_3N_4. Just after full densification, the TiN particles must reside primarily in the intergranular region as a result of minimized Si_3N_4 grain growth allowed during the very fast densification (99% density was reached in ~200 s), as evinced by both comparing the grain sizes of the dense material after 460 s hot-pressing with the initial Si_3N_4 particle size, and the actual distribution of TiN in the dense materials hot-pressed for 460 s (Fig. 6). With continuing heating some TiN grains become encapsulated by growing Si_3N_4 and Si_2N_2O grains giving an intragranular distribution, as a result of grain-boundary movement, and some TiN grains are trapped at grain boundaries and attached to them, to produce intergranular distribution.

During Si_3N_4 grain growth, whether a TiN inclusion is attached to a grain boundary to exert a pinning effect or breaks away from the boundary leaving behind an intragranular TiN particle, can be related to the maximum permissible velocity of the inclusion, V_p, and the grain boundary, V_b, as described by Brook [28]. When $V_p \geqslant V_b$, the inclusion stays on the grain boundary and exerts a pinning effect. This possibly gives rise to a fine-grained microstructure with intergranular inclusions. On the other hand, when $V_p < V_b$, the inclusion can break away from the grain boundary. The pinning effect is then lost, resulting in a large-grained microstructure with intragranular inclusions.

These velocities can be treated as force mobility products

$$V_p = F_p M_p \tag{11}$$

$$V_b = F_b' M_b \tag{12}$$

where M_p and M_b are the mobility of inclusion and grain boundary, and F_p and F_b' are the forces acting on the inclusion and grain boundary. The force F_b' consists of two parts, F_b, the force arising from the curvature of the boundary, and NF_p the drag force of the N attached inclusions, thus

$$V_p = F_p M_p \tag{13}$$

and

$$V_b = (F_b - NF_p) M_b \tag{14}$$

Because V_p and V_b are proportional to M_p and M_b, respectively, the relative ratio of M_p/M_b is important in controlling grain growth. A large M_p/M_b corresponds to the situation of inclusion attachment to the grain boundary. It has been observed that M_p is directly related to the inclusion size, r, as

$$M_p \propto r^{-n} \tag{15}$$

where $n = 3$ for volume diffusion and $n = 4$ for interfacial diffusion-dominated material transport around the inclusion particles [29]. Equation 15 indicates that, with the same M_b, the smaller the inclusion size, the greater is the possibility of grain-boundary attachment of the inclusion. In other words, in a given material, if the inclusions have a wide size distribution, the relatively coarse inclusions have a large likelihood of being intragranularly distributed, and the finer ones have an intergranular distribution, as has been shown for oxide ceramics [30–32]. Observations of the TiN

distribution in the 5.4 ks hot-pressed materials indicate a predominant intergranular distribution (Fig. 6). This can probably be related to the overall fine size of the TiN grains. A few relatively coarse (~200 nm) TiN grains are, however, intragranular, as would be predicted (Fig. 8).

From a consideration of the thermal properties of $Si_3N_4$and TiN, a stress field, or even microcracks, could be expected in the vicinity of the Si_3N_4–TiN interface. The stress field arising from the thermal expansion mismatch and Young's modulus difference in a two-phase material can be expressed using spherical coordinates [32]:

in the matrix

$$\begin{aligned}\sigma_{rrm} &= -2\sigma_{\theta\theta m} \\ &= -2\sigma_{\phi\phi m} \\ &= -\frac{P_{con}R_{in}^3}{r_x^3}\end{aligned} \tag{16}$$

and in the inclusion

$$\begin{aligned}\sigma_{rri} &= 2\sigma_{\theta\theta i} \\ &= 2\sigma_{\phi\phi i} \\ &= -P_{con}\end{aligned} \tag{17a}$$

with

$$P_{con} = \frac{(\alpha_p - \alpha_m)\Delta T E_m}{(1+\nu_m)/2 + E_m(1-2\nu_p)/E_p} \tag{17b}$$

where r_x is the distance from the centre of the inclusion ($r_x \geqslant R_{in}$), R_{in} is the radius of the inclusion, E is the Young's modulus, ν is Poisson's ratio. The subscripts m and p refer to the matrix and particulate phases, respectively, $\Delta\alpha = (\alpha_p - \alpha_m)$ and $\Delta T = (T_g$ – room temperature), where T_g is defined as the temperature below which the residual stress is no longer relaxed by viscous deformation or diffusion. The residual stresses in the matrix decrease with increasing distance from the inclusion. The stresses on the interface and within the inclusion have the maximum values. For the Si_3N_4–TiN composite, $\alpha_{TiN} > \alpha_{Si_3N_4}$, and the radial components σ_{rri} and σ_{rrm} are tensile whereas the tangential components are compressive. The maximum stress level can be estimated using, $E_{Si_3N_4} =$ 300 GPa, $E_{TiN} = 469$ GPa, $\alpha_{Si_3N_4} = 3.25\,MK^{-1}$, $\alpha_{TiN} = 8.0\,MK^{-1}$, $\nu_{Si_3N_4} = \nu_{TiN} = 0.25$, $\Delta T = 1200\,°C$ [1]. A residual tensile stress of ~1.8 GPa within the TiN particles and at the interface between Si_3N_4 and TiN can be developed. This value is about 6% of the theoretical for Si_3N_4 (the theoretical strength is estimated from $\sigma_{th} = E/10$, E is Young's modulus [33]). However, such a high stress exceeds the measured bend strength of Si_3N_4 bulk materials. A possible consequence of the residual stress should be microcraking within the TiN grain or along the interface. TEM observations show, however, no microcracks in this region. The glass film (Fig. 9) sandwiched between the TiN and Si_3N_4 grains may be expected to release partially the residual stress before the glass transition. If we choose a glass transition temperature of 800 °C giving $\Delta T = 775\,°C$, the residual tensile stress is then ~1.2 GPa. This is still a very high value. However, the commonly observed high density of dislocations causing damaging features within TiN particles in the Si_3N_4–TiN composite in this study, and with others for Si_3N_4–TiN composite [34], might be explained by the very high residual tensile stress within the TiN grains.

It is also well-established that in two-phase particulate composites, spontaneous microcracking depends on the inclusion size. There is a critical inclusion size, D_c, and for an inclusion size larger than this, microcracks should be induced, or only a stress field was induced. The critical inclusion size has been estimated from the following equation [32]

$$D_c = \eta K_{IC}^2 \left[\frac{1+\nu_m}{2} + \frac{E_m(1-2\nu_p)}{E_p}\right]^2 \Big/ (E_m \Delta\alpha\Delta T)^2 \tag{18}$$

where η is a constant depending on the fracture mode ranging from 2–8. K_{Ic} is the fracture toughness of the microcracking site. The calculated value of D_c is 4 μm for the Si_3N_4–TiN composite. Thus for the materials prepared in this study the TiN inclusions are much smaller than the critical size, and no microcracking would be expected.

Concerning the interface compatibility between the Si_2N_2O and the Si_3N_4 grains, a similar calculation made with $\alpha_{Si_2N_2O} = 3.0\,MK^{-1}$, and $E_{Si_2N_2O} =$ 220 GPa [35], gives a maximum residual stress of ~ 70 MPa. This value is not high enough to cause damage in the material.

4.3. Residual glass phase

The crystallization of a glass segregated at a grain boundary has been predicted by Raj and Lange [36] to be thermodynamically more difficult than the crystallization of a bulk glass of the same composition. Because glass at a multi-grain junction can sustain only a hydrostatic stress, the strain energy resulting during crystallization depends on the difference in the specific volumes of the crystalline and glass phases, the bulk modulus of the two phases, and the size of the crystal forming in the grain junction. The minimum in the free energy of transformation occurs for a crystal size that is close to one-half of the glass pocket size. This minimum characterizes the elastic constraint on crystal growth which should lead to only limited crystallization of the glass, with crystallization more likely in the larger pockets. Experimentally they demonstrated in Si_3N_4 that glass segregated in boundary cavities should crystallize only partially and that the glass segregated at four grain junctions is more likely to crystallize than glass segregated at three grain junctions. Observations made by TEM of 460 s and 5.4 ks hot-pressed materials support those results. In the 460 s hot-pressed sample, three-grain junction glass pockets could be identified and an intergrain boundary film of several nanometers could be resolved by HRTEM (Figs 9 and 10). With prolongment of hot-

pressing to 5.4 ks, some of the larger pockets (typically ~100 nm) become filled with a crystallized phase typical of a conical morphology accommodating the grain junction face. HRTEM observation indicates, however, that the crystallization is not complete, and leaves a glass film and small pockets of several nanometres in dimension. In the Y_2O_3 sintered sialon system, mullite is typically precipitated from the glass, following heterogeneous nucleation on the surfaces of sialon grains [37]. However, in the present case, there was no evidence of mullite. The small size of the crystallized phase made it very difficult to carry out a structural analysis under TEM. Based on the composition of the glass, because it is SiO_2 rich, the crystallizing phase is possibly silicon oxynitride (Si_2N_2O).

5. Conclusions

Al_2O_3–TiO_2–SiO_2 is an effective hot-pressing densification system for Si_3N_4. Although the reduction of TiO_2 to $TiO_{(2-x)}$ and finally nitridation to TiN make the role of TiO_2 during the densification process complex, the reduction and nitridation of TiO_2 is expected to be beneficial for the densification of Si_3N_4 by providing an *in situ* source of SiO_2, and also possibly by reducing the liquid-formation temperature within the densification system of Al_2O_3–SiO_2–$TiO_{(2-x)}$. The conversion of fine TiO_2 particles to TiN provides an alternative way for making Si_3N_4–TiN composites with nano-dimension TiN particles.

On densification, the oxide additive phase is redistributed. The Al_2O_3 is redistributed on a finer scale because of the solid solution of Al_2O_3 in the β′-sialon lattice; the TiO_2 is redistributed on a coarser scale, possibly because of the TiO_2 particle coarsening, and the conversion of TiO_2 to TiN through a solution and reprecipitation process, permitting some grain growth. The conversion of TiO_2 to TiN is fast. The overall life-time of TiO_2 above 1100 °C is estimated to be ~1.3 ks. Conversion of TiO_2 to TiN is believed to occur through two routes: the reduction and nitridation of particulate TiO_2, and the precipitation of TiN from an aluminium–silicate liquid phase as a result of the reduction and nitridation of dissolved TiO_2.

In the β′-sialon TiN nano-composite, the TiN particles are primarily located intergranularly in a β′-sialon matrix. Thin (2–3 nm) films of amorphous material may be an important feature of the microstructure, in that this film separates the β′-sialon grains from the TiN grains, and the β′-sialon grains from the unreacted α-Si_3N_4 grains.

As densification proceeds, the bulk glass segregated in three- and multi-grain junctions was crystallized to Si_2N_2O and hence only leaves a thin amorphous film of several nanometres separating the crystalline phases.

Acknowledgements

The author thanks Dr F. L. Riley for critical comments on the work.

References

1. A. BELLOSI, S. GUICCIARDI and A. TAMPIERI, J. Eur. Ceram. Soc. **9** (1992) 89.
2. K. KISH and S. UMEBAYASHI, *J. Ceram. Soc. Jpn* **96** (1988) 725.
3. T. MAH, *Bull. Am. Ceram. Soc.* **60** (1981) 1229.
4. F. F. LANGE, *J. Am. Ceram. Soc.* **56** (1973) 445.
5. *Idem, ibid.* **72** (1989) 3.
6. R. RIEDIL, K. STRECKER and G. PETZOW, *ibid.* **72** (1989) 2071.
7. D. N. OVREBOE, S. K. BISWAS, F. CASTRO and F. L. RILEY, in "4th International Symposium on Ceramic materials and Components for Engines", edited by R. Carlsson, T. Johasson and L. Kahlman (Elsevier Applied Science, London, 1991) pp. 315–23.
8. C. M. WANG and F. L. RILEY, *J. Eur. Ceram. Soc.* **10** (1992) 83.
9. C. P. GAZZARA and D. R. MESSIER, *Bull. Am. Ceram. Soc.* **56** (1977) 777.
10. K. ICHIKAWA, in "Silicon nitride-I" edited by S. Somiya, M. Mitomo and M. Yshimura (Elsevier Applied Science, London, 1990) pp. 107–16.
11. B. BERGMAN and H. HEPING, *J. Eur. Ceram. Soc.* **6** (1990) 3.
12. T. EKSTROM, P. O. KALL, M. NYGREN and P. O. OLSSON, *J. Mater. Sci.* **24** (1989) 1853.
13. D. A. BONNEL, M. RUHLE and T. Y. TIEN, *J. Am. Ceram. Soc.* **69** (1986) 623.
14. M. H. LEWIS, C. J. REED and N. D. BUTLER, *Mater. Sci. Eng.* **71** (1985) 87.
15. W. D. KINGERY, *J. Appl. Phys.* **30** (1959) 301.
16. S. HAMPSHIRE and K. H. JACK, *Proc. Br. Ceram. Soc. Spec. Ceram. 7* **31** (1981) 37.
17. S. HAMPSHIRE, R. A. L. DREW and K. H. JACK, *Phys. Chem. Glasses* **26** (1985) 182.
18. M. TRIGG, *J. Am. Ceram. Soc.* **63** (1980) 103.
19. W. Y. LI and F. L. RILEY, *J. Eur. Ceram. Soc.* **8** (1991) 345.
20. A. D. STALIOS, J. LUYTEN, C. D. HEMSLEY, F. L. RILEY and R. J. FORDHAM, *ibid.* **7** (1991) 75.
21. K. H. JACK, *Met. Technol.* **9** (1982) 297.
22. M. B. TRIGG and E. R. McCARTNEY, *J. Am. Ceram. Soc.* **64** (1981) C153.
23. N. S. JAMEEL and D. P. THOMPSON, in "British Ceramic Society Proceedings, Special Ceramics 8", edited by S. P. Howlett and D. P. Thompson, (British Ceramic Society, London, 1988) pp. 95–108.
24. W. K. TREDWAY and S. H. RISBUD, *J. Mater. Sci. Lett.* **4** (1985) 31.
25. I. SEKERCIOGULU and R. R. WILLS, *J. Am. Ceram. Soc.* **62** (1979) 590.
26. W. G. STALEY and G. W. BRINDLEY, *ibid.* **52** (1969) 616.
27. R. F. DAVIS and J. A. PASK, *ibid.* **55** (1972) 525.
28. R. J. BROOK, in "Treatise on materials science and technology", Vol. 9, edited by F. F. Wang (Academic Press, New York, 1976) pp. 331–64.
29. P. G. SHEWMAN, *Trans. Metall. Soc. AIME* **230** (1964) 1134.
30. F. F. LANGE and M. M. HIRLINGER, *J. Am. Ceram. Soc.* **67** (1984) 164.
31. L. A. XUE, K. MEYER and I. W. CHEN, *ibid.* **75** (1992) 822.
32. D. J. MAGLEY, R. A. WINHOLTZ and K. T. FABER, *J. Am. Ceram. Soc.* **73** (1990) 1641.
33. R. W. DAVIDGE, in "Mechanical behaviour of ceramics", (Cambridge University Press, Cambridge, 1980) pp. 28–32.
34. W. Y. LI, PhD thesis, University of Leeds (1992).
35. P. BOCH and J. C. GLANDUS, in "Progress in nitrogen ceramics", edited by F. L. Riley (Martinus Nijhoff, The Hague, 1983). pp. 589–94.
36. R. RAJ and F. F. LANGE, *Acta Metall* **29** (1981) 1993.
37. D. V. SZABO, G. H. CAMPBELL, J. BRULELY, M. J. HOFFMANN and M. RUHLE, *J. Am. Ceram. Soc.* **75** (1992) 249.
38. K. H. JACK, *J. Mater. Sci.* **11** (1976) 1135.

Received 21 December 1993
and accepted 3 February 1994